CHAPTER – 5

Microstructure, mechanical, and tribological behaviour of a Ti-Zr-Nb-Mo-Fe-Cr based bio-CCA

5.1 Background

As discussed in the literature review chapter, implant biomaterials are primarily used in load-bearing orthopedic applications, including hip, knee, spinal, and shoulder joints, dental roots, and cardiovascular stents. Among these, spinal, hip, and knee replacement implants are used most extensively [12]. Human joints are susceptible to degenerative diseases such as arthritis, which lead to pain and reduced functionality. These conditions contribute to the deterioration of the bone's mechanical properties, mainly due to excessive loading or the absence of natural biological self-healing mechanisms [8]. Presently, conventional metallic implant materials used in clinical application include 316L stainless steel, CoCrMo alloys, Mg alloys, and Ti and its alloys. However, these materials often exhibit poor mechanical and tribological properties, along with a significantly high elastic modulus. Therefore, these materials are not suitable for long-term clinical application, usually necessitating revision surgeries.

In line with the aforementioned background, the present chapter focuses on the development of a novel Ti-Zr-Nb-Mo-Fe-Cr-based bio-CCA that combines both refractory and non-refractory elements, with the aim of addressing the limitations of the previously developed $Ti_{10}Nb_{30}Mo_{20}Fe_{20}Cr_{20}$ CCA discussed in the previous chapter. The primary objective is to achieve a unique combination of low density and elastic modulus, high strength and superior wear resistance, and sufficient corrosion resistance and biocompatibility. Out of these, the present chapter focuses on density, elastic modulus, strength and wear behaviour, while corrosion and biocompatibility are discussed in the next chapter.

The results and discussion presented in the current chapter are divided into several subsections. The first subsection outlines the alloy design strategy and presents the microstructural characterization of the fabricated CCA in its as-cast condition. The second subsection focuses on the microstructural evolution during annealing, demonstrating the changes observed in the alloy upon annealing treatment. The third subsection presents an evaluation of the mechanical properties of both as-cast and annealed CCA samples using microindentation measurements and elastoplasticity analysis. The fourth and fifth subsections detail the tribological performance, including reciprocating wear behavior and worn surface analysis for both alloy conditions.

5.2 Results

5.2.1 Alloy design and microstructural characterization of as-cast bio-CCA

The aim of alloy design is to achieve a unique combination of desirable properties, including low density, reduced elastic modulus, high strength with sufficient plasticity, excellent corrosion and wear resistance, and biocompatibility. In the study presented in the previous chapter, we successfully achieved low density, high strength, and outstanding corrosion resistance; however, the elastic modulus remained relatively high. Therefore, to address this, we tailored the composition by adding Zr into our previous alloy composition, aiming to reduce the elastic modulus and enhance cytocompatibility while maintaining strength and corrosion resistance, leading to the design of a new Ti-Zr-Nb-Mo-Fe-Cr-based CCA. The main reasons for choosing Zr are its ability to reduce the elastic modulus, density, and magnetic susceptibility of the alloy [191-192]. Additionally, Zr is known for its excellent biocompatibility and its ability to form a stable, non-toxic, and corrosion-resistant oxide layer

(ZrO_2) in physiological environments, thereby minimizing metal ion release from the alloy surface. Also, Zr has been shown to promote osteoblast activity, enhance cell adhesion, and support bone integration.

The CALPHAD-based modelling using ThermoCalc software was used to perform a stepped equilibrium phase diagram calculation. Based on the predicted phase evolution and stability over a range of temperatures, the composition $Ti_{35}Zr_{35}Nb_{15}Mo_5Fe_5Cr_5$ was identified as the optimized alloy composition. The resulting stepped equilibrium diagram of $Ti_{35}Zr_{35}Nb_{15}Mo_5Fe_5Cr_5$ CCA, shown in Figure 5.1 (a), was generated using the SSOL database version 6 and illustrates all thermodynamically stable phases and their respective fractions across the temperature range. At room temperature, ThermoCalc predicts the presence of three major phases: BCC1 (enriched in Nb, Zr, Ti, and Mo), BCC2 (primarily of Zr and Ti), and the Laves phase (containing Cr, Zr, and Ti).

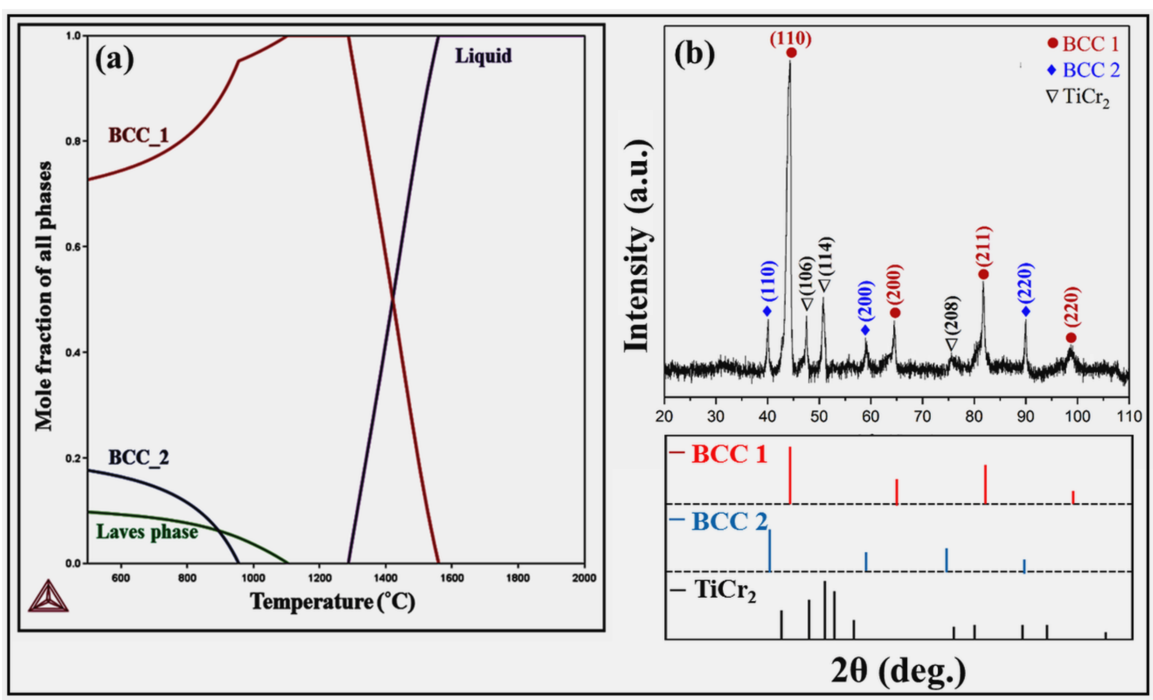

Figure 5.1 (a) Stepped equilibrium calculation diagram obtained from ThermoCalc (b) XRD pattern with standard peak positions indicated below of $Ti_{35}Zr_{35}Nb_{15}Mo_5Fe_5Cr_5$ CCA.

The theoretical density of the $Ti_{35}Zr_{35}Nb_{15}Mo_5Fe_5Cr_5$ CCA, calculated using the rule of mixtures, was estimated at 6.37 g/cm³. In comparison, the experimentally measured density of the as-cast alloy was 6.31 ± 0.02 g/cm³. Notably, this CCA demonstrates a lower density than many reported biocompatible alloys, including both conventional alloys and bio-HEAs/CCAs [42,67,69,121,193], and is even lower than our previously developed $Ti_{10}Nb_{30}Mo_{20}Fe_{20}Cr_{20}$ CCA.

Figure 5.1 (b) exhibits the XRD pattern of the as-cast $Ti_{35}Zr_{35}Nb_{15}Mo_5Fe_5Cr_5$ CCA. The XRD analysis indicates that the alloy predominantly consists of a BCC1 phase, along with minor amounts of BCC2 and a $TiCr_2$-type Laves phase. Notably, these experimentally observed phase constitutions are in good agreement with phase predictions obtained from ThermoCalc software, thereby validating the accuracy of the CALPHAD modelling. The lattice parameters for the BCC1 and BCC2 phases are 3.360 ± 0.004 Å and 3.616 ± 0.002 Å, respectively, while the $TiCr_2$-type Laves phase has lattice constants of a = 4.912 Å and c = 7.961 Å. The corresponding phase fractions, calculated using Equations 3.3–3.5, are 75.35% for BCC1, 12.63% for BCC2, and 12.02% for the $TiCr_2$ phase.

Figure 5.2 (a and b) shows the optical and SEM microstructures of the as-cast $Ti_{35}Zr_{35}Nb_{15}Mo_5Fe_5Cr_5$ CCA. The alloy exhibits a characteristic dendritic morphology, with the light grey areas corresponding to dendritic regions and the darker grey areas representing the interdendritic zones. This dendritic structure results in elemental segregation, as elements with higher melting points tend to solidify earlier and segregate within the dendritic regions, while those with lower melting points solidify later and segregate in the interdendritic areas [65].

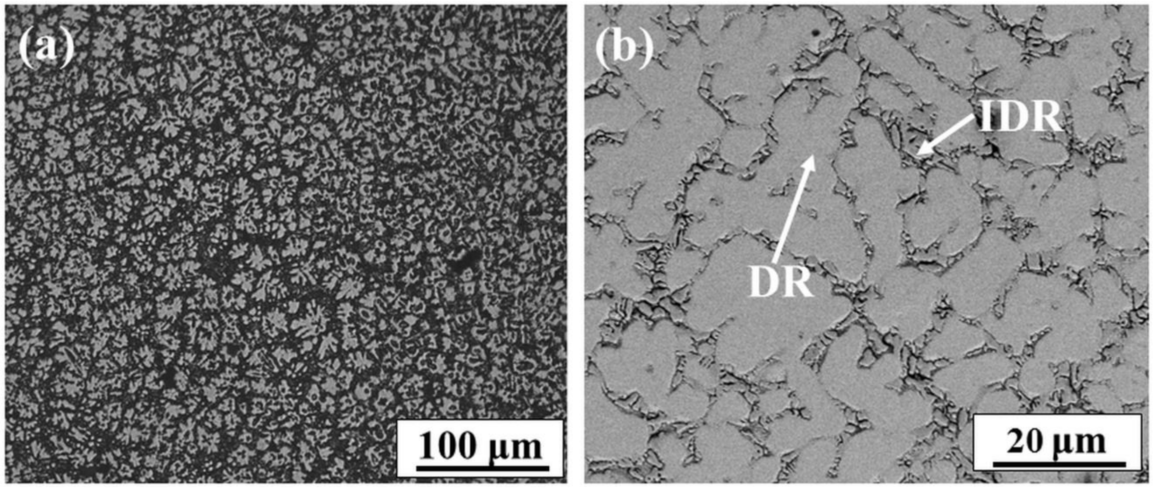

Figure 5.2 (a) optical and (b) SEM image of as-cast $Ti_{35}Zr_{35}Nb_{15}Mo_5Fe_5Cr_5$ CCA; IDR and DR shows interdendritic and dendritic region, respectively.

The EDS elemental mapping of the as-cast $Ti_{35}Zr_{35}Nb_{15}Mo_5Fe_5Cr_5$ CCA, shown in Figure 5.3, reveals a non-uniform distribution of the constituent elements. The dendritic regions are enriched with high-melting elements like Mo and Nb, while lower-melting elements preferentially segregate into the interdendritic regions. In contrast, Zr is distributed more uniformly across the microstructure.

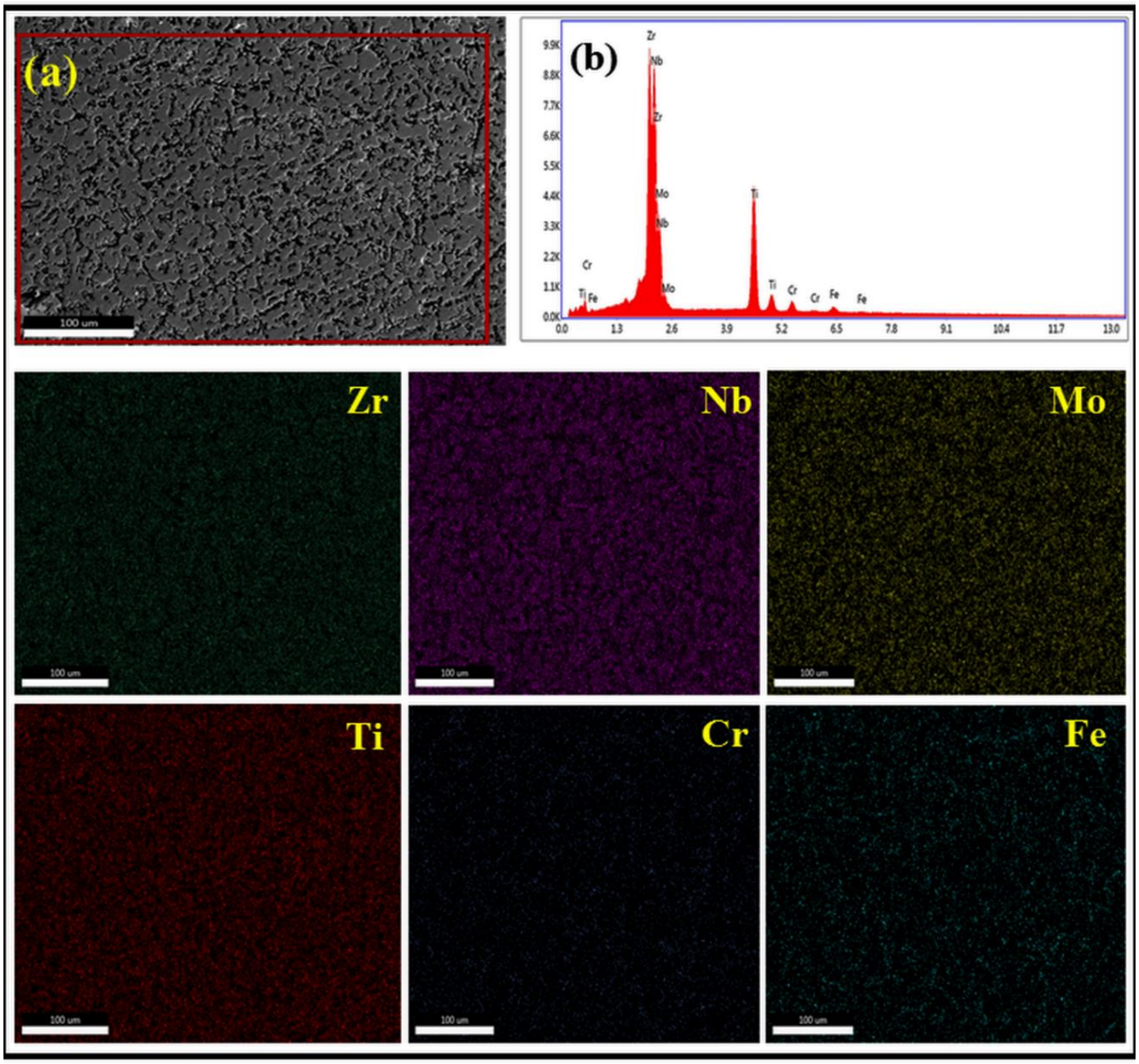

Figure 5.3 EDS compositional analysis of as-cast $Ti_{35}Zr_{35}Nb_{15}Mo_{5}Fe_{5}Cr_{5}$ CCA via area spectrum along with elemental mapping.

5.2.2 Microstructural characterization of annealed bio-CCA

As mentioned earlier, vacuum arc-melted alloys undergo elemental segregation and internal stresses as a result of the high cooling rate. Therefore, annealing treatment was carried out to reduce these issues in the as-cast alloy. Figure 5.4 shows the XRD patterns of the $Ti_{35}Zr_{35}Nb_{15}Mo_{5}Fe_{5}Cr_{5}$ CCA annealed at 700°C, 900°C, and 1100°C for 20 hours. The results indicate that the BCC1 and BCC2 solid solution phases remain stable across all annealing conditions. In contrast, the peak intensity of the Laves phase increases progressively with annealing temperature, implying a corresponding increase in its phase fraction. Notably, the amount of Laves phase increases from 15.21% at 700°C to 17.03% at 900°C, and further to 20.59% at 1100°C.

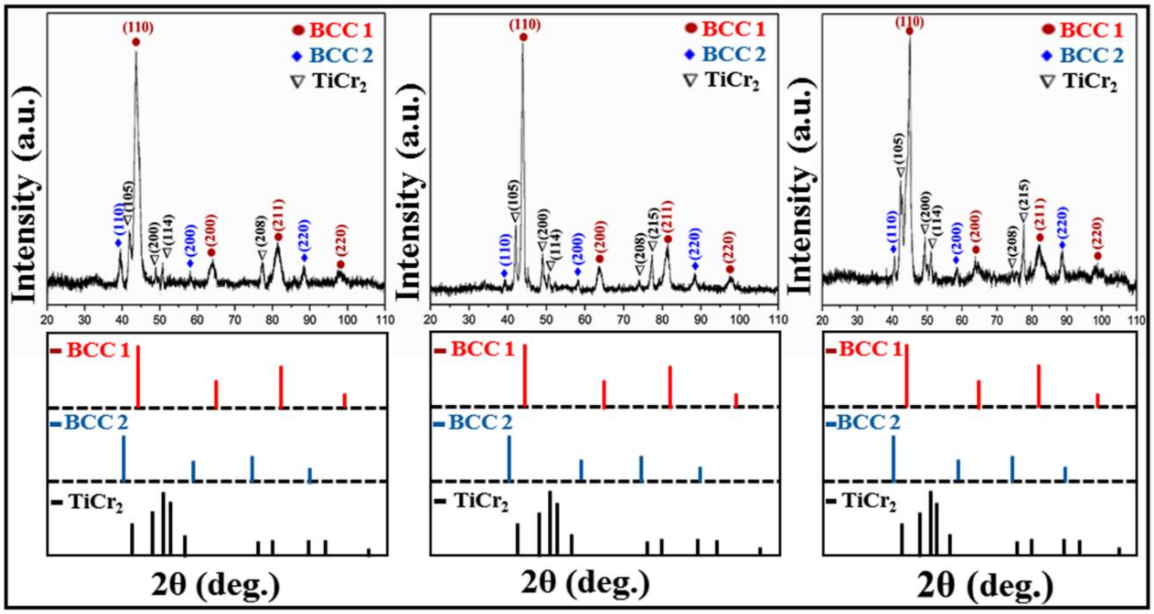

Figure 5.4 XRD pattern with standard peak positions for the $Ti_{35}Zr_{35}Nb_{15}Mo_5Fe_5Cr_5$ CCA annealed at various temperatures: (a) 700°C, (b) 900°C, and (c) 1100°C.

Figure 5.5 shows the optical and SEM microstructures of the $Ti_{35}Zr_{35}Nb_{15}Mo_5Fe_5Cr_5$ CCA annealed at 700°C, 900°C, and 1100°C. Specifically, Figures 5.5 (a), (c), and (e) exhibit the optical micrographs, while Figures 5.5 (b), (d), and (f) show the corresponding SEM images. The annealing process led to a notable transformation of the dendritic morphology observed in the as-cast condition (Figure 5.2) into a predominantly globular morphology. The CCA annealed at 700 °C shows an irregular or equiaxed grain morphology, with dendrite width increasing from 8.15 ± 0.80 µm in the as-cast state to 11.95 ± 1.24 µm. In contrast, specimens annealed at 900 °C and 1100 °C exhibit a globular microstructure, with average grain sizes of approximately 14.41 ± 0.79 µm and 17.56 ± 0.66 µm, respectively. In addition, as the annealing temperature increases, both the size and number density of Laves phase particles increase. These observations indicate that high annealing temperature promotes microstructural coarsening, primarily driven by grain growth mechanisms.

The Laves phase particles are barely visible in the microstructure of the CCA annealed at 700 °C (Figure 5.5 (a–b)), owing to their fine size. In contrast, annealing at 900 °C and 1100 °C results in a noticeable coarsening of these particles and exhibits an oblate morphology, as evident in the microstructures shown in Figure 5.5 (c–f). Additionally, XRD analysis reveals a progressive increase in the volume fraction of the Laves phase with increasing annealing temperatures, indicated by the intensified Laves phase peaks in Figure 5.4. Notably, the combined insights from XRD and SEM analyses confirm the absence of any new phase formation across all annealing conditions, with the BCC solid solution phase remaining predominant. These results suggest that the $Ti_{35}Zr_{35}Nb_{15}Mo_5Fe_5Cr_5$ CCA possesses outstanding structural stability.

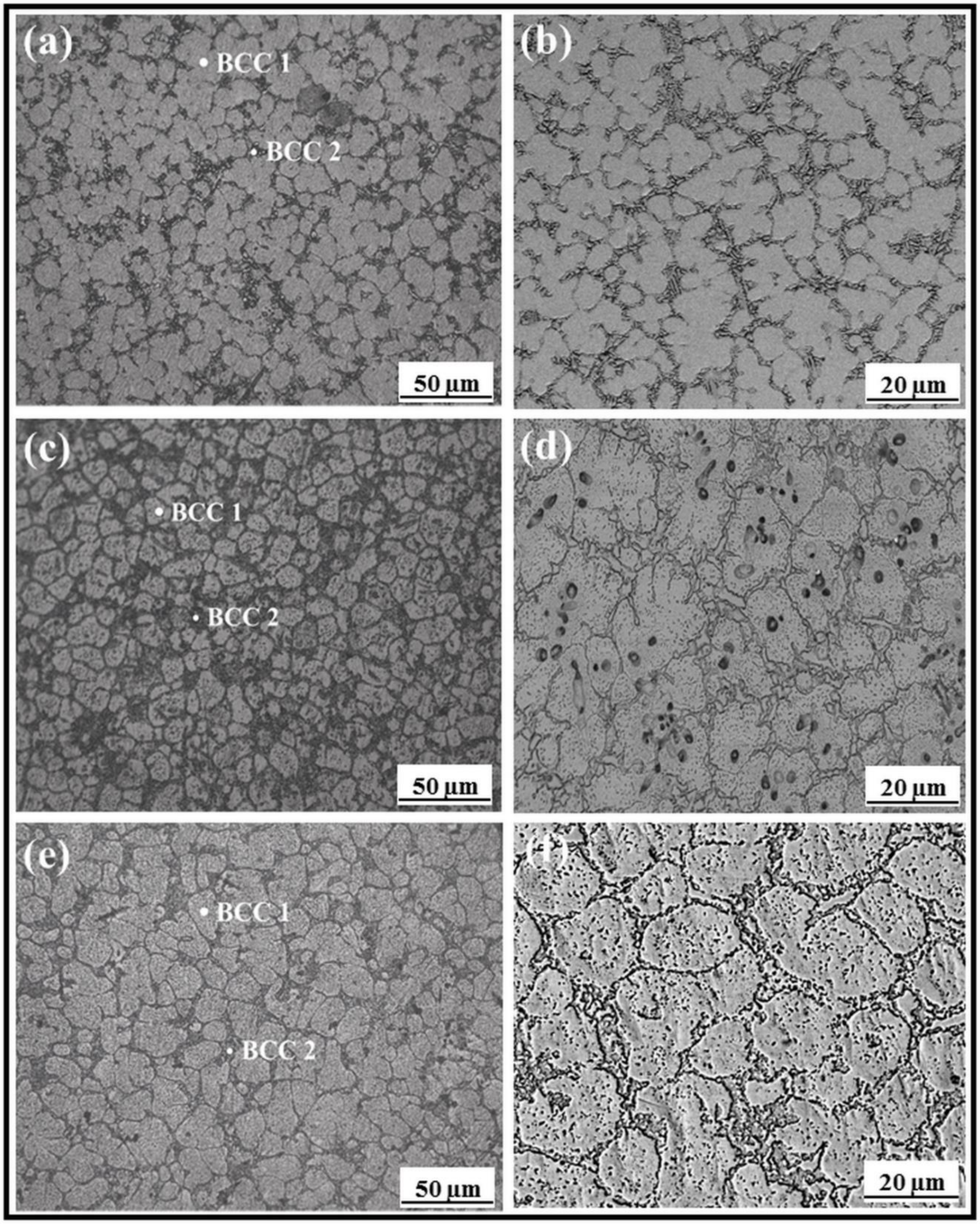

Figure 5.5 Optical and SEM microstructure of the $Ti_{35}Zr_{35}Nb_{15}Mo_5Fe_5Cr_5$ CCA annealed at various temperatures (a & b) 700°C, (c & d) 900°C, and (e & f) 1100°C.

5.2.3 Mechanical behaviour of the $Ti_{35}Zr_{35}Nb_{15}Mo_5Fe_5Cr_5$ CCA

5.2.3.1 Instrumented micro-indentation test of $Ti_{35}Zr_{35}Nb_{15}Mo_5Fe_5Cr_5$ CCA

The P - h curves for both the as-cast and annealed $Ti_{35}Zr_{35}Nb_{15}Mo_5Fe_5Cr_5$ CCA specimens are shown in Figure 5.6 (a). As illustrated in Figure 5.6 (b), the as-cast alloy exhibits an average hardness of 618.39 ± 9.26 HV and an elastic modulus of 97.32 ± 3.58 GPa. Notably, both the hardness and elastic modulus increase significantly with increasing annealing temperatures. This enhancement is likely due to the substantial precipitation of the hard Laves phase during annealing, compared to the as-cast state. In particular, the sample annealed at 1100˚C achieves an average hardness of 833.08 ± 7.58 HV and an elastic modulus of 115.62 ± 3.68 GPa. XRD analysis (Figures 5.1 (b) and 5.4) confirms that the volume fraction of the Laves phase within the BCC solid solution increases with annealing temperature. This phase evolution contributes to the overall mechanical strengthening through a combined mechanism of solid solution strengthening from the BCC matrix and precipitation strengthening from the Laves phase. Similar observations were reported by Zhang et al. [92] and Shun et al. [194], who observed that annealing led to increased hardness in $CoCrMoNbTi_{0.4}$ and $CoCrFeNiTi_x$ HEAs.

The elastic modulus of the $Ti_{35}Zr_{35}Nb_{15}Mo_5Fe_5Cr_5$ CCA is not only substantially lower than that of our previously investigated composition, $Ti_{10}Nb_{30}Mo_{20}Fe_{20}Cr_{20}$, but also considerably lower than those of conventional implant materials such as 316L stainless steel (E = 195 GPa) and CoCrMo alloy (E = 222 GPa). Notably, the elastic modulus is reasonably comparable to that of cp-Ti and other Ti-based alloys [42,75], which are known for their favorable bone-compatible elastic modulus. In addition, this CCA exhibits a significantly lower elastic modulus than several reported biocompatible HEAs, including TiMoNbTaW, TiMoNbTaWCr [69], TiZrNbTaMo [41], and TiAlFeCoNi [75].

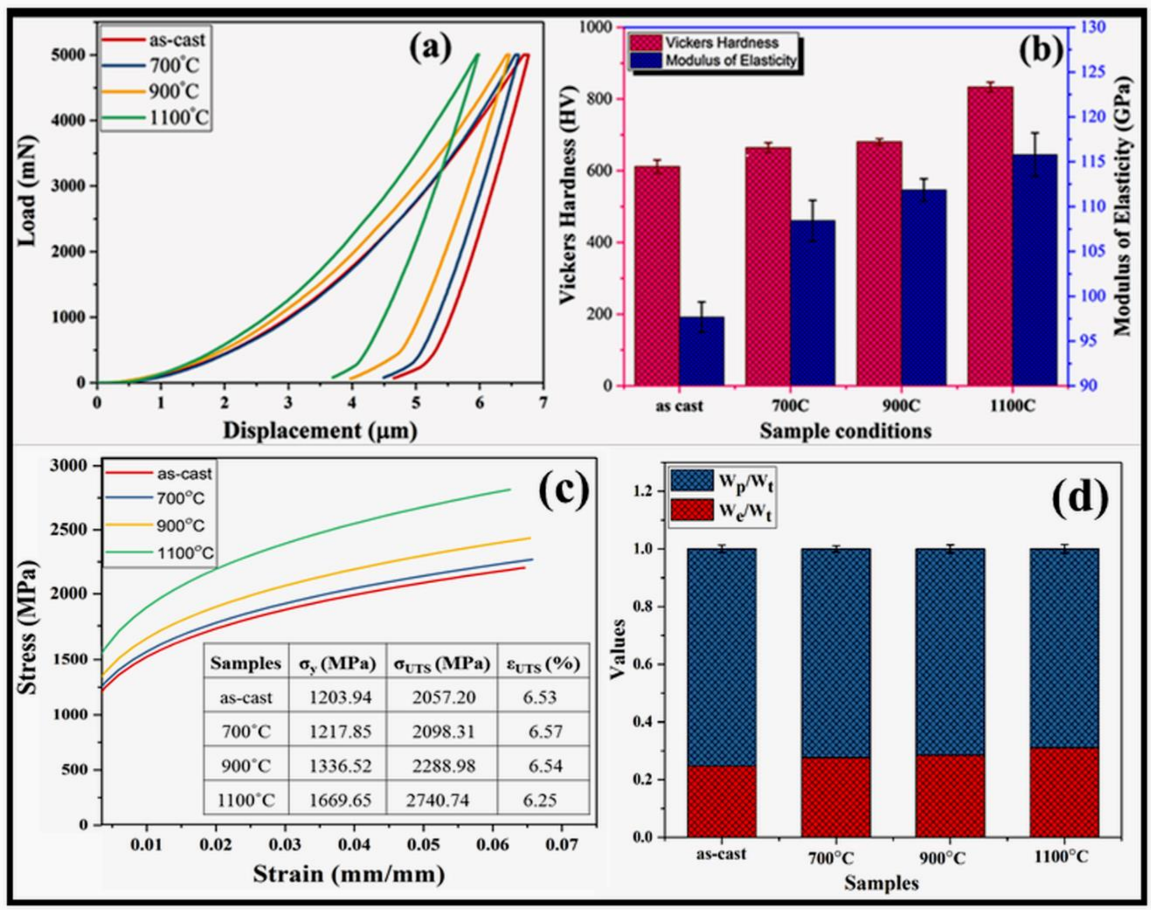

Figure 5.6 Instrumented micro-indentation and elastoplastic response of the $Ti_{35}Zr_{35}Nb_{15}Mo_5Fe_5Cr_5$ CCA: (a) Load–displacement (P–h) curves; (b) average hardness and elastic modulus; (c) calculated stress–strain curve; (d) elastic recovery ratio (W_e/W_t) and plasticity index (W_p/W_t).

5.2.3.2 Elastoplastic characteristics of the $Ti_{35}Zr_{35}Nb_{15}Mo_5Fe_5Cr_5$ CCA

The hardness values obtained from instrumented micro-indentation confirm the considerable strength of the $Ti_{35}Zr_{35}Nb_{15}Mo_5Fe_5Cr_5$ CCA, with the highest values observed in the sample annealed at 1100°C. However, evaluating the alloy's plasticity is equally important, as the increase in hardness from the as-cast to the annealed state is largely attributed to the presence of greater amount of the hard Laves phase (which is also brittle).

Therefore, the micro-indentation data was used to estimate and analyze the elastoplastic behaviour by numerically solving Equations 3.9 to 3.14, as detailed in the Materials and Methods chapter (section 3.6.2). This analysis provided the elastoplastic parameters and the corresponding stress–strain response of the alloy, as shown in Figure 5.6 (c).

The yield strength (YS) and ultimate tensile strength (UTS) of both the as-cast and annealed CCA samples show good correlation with their respective hardness values. For the alloy annealed at 1100°C, the YS and UTS values are 1669.65 ± 24.79 MPa and 2740.74 ± 28.64 MPa, respectively. In comparison, the as-cast alloy exhibits lower values, with a YS of 1203.94 ± 30.28 MPa and a UTS of 2057.20 ± 32.47 MPa. Remarkably, the strain hardening exponent remains nearly constant for as-cast and annealed conditions ($n \approx 0.26$). These results suggest that increasing the annealing temperature enhances the alloy's strength without significantly compromising its plastic strain.

Figure 5.6 (d) also illustrates the elastic recovery and plasticity index for both the as-cast and annealed $Ti_{35}Zr_{35}Nb_{15}Mo_5Fe_5Cr_5$ CCA. The elastic recovery index (W_e/W_t) increases from the as-cast to the annealed state, with the alloy annealed at 1100°C exhibiting the highest W_e/W_t value. This enhancement is advantageous for impact resistance, as a higher elastic recovery index is associated with better resistance to impact loading [159]. Importantly, the elastoplastic stress-strain analysis reveals that the plasticity index (W_p/W_t) decreases only marginally, despite the increased volume fraction of the hard Laves phase in the annealed sample. This indicates that the alloy retains a favorable combination of high strength and adequate plasticity.

5.2.4 Tribological behaviour of $Ti_{35}Zr_{35}Nb_{15}Mo_5Fe_5Cr_5$ CCA

Figure 5.7 depicts the average coefficient of friction (COF) versus applied normal load for the $Ti_{35}Zr_{35}Nb_{15}Mo_5Fe_5Cr_5$ CCA under wet sliding conditions in simulated body fluid solution. The results demonstrate that the COF value varies significantly with changes in the applied load (i.e., 10 N, 15 N, 20 N, and 25 N). At 10 N, the as-cast CCA exhibits the highest COF of 0.59. However, as the normal load increases, the COF gradually decreases, reaching a minimum of 0.41 at 25 N. This reduction in COF with increasing load is likely due to mating asperity flattening or the formation of rounded wear debris during sliding. A similar trend was observed by Shittu et al. in a biocompatible MoNbTaTiZr HEA [112].

At higher normal loads, a large amount of metallic oxide formation may also contribute to the decrease in COF. A similar trend is observed in annealed CCA specimens, where the COF decreases with increasing applied load. In addition, the COF further decreases with increasing annealing temperature, likely due to the corresponding enhancement in alloy hardness. As the hardness increases at higher annealing temperatures, the COF is consequently reduced. This correlation between increased hardness and lower COF in simulated body fluid has also been reported by Li et al. for the biocompatible TiTaZrNbMo alloy [195]. Generally, the COF of the metallic materials is affected by several factors, such as the applied normal load, the hardness of the contacting surfaces, and their surface conditions [196].

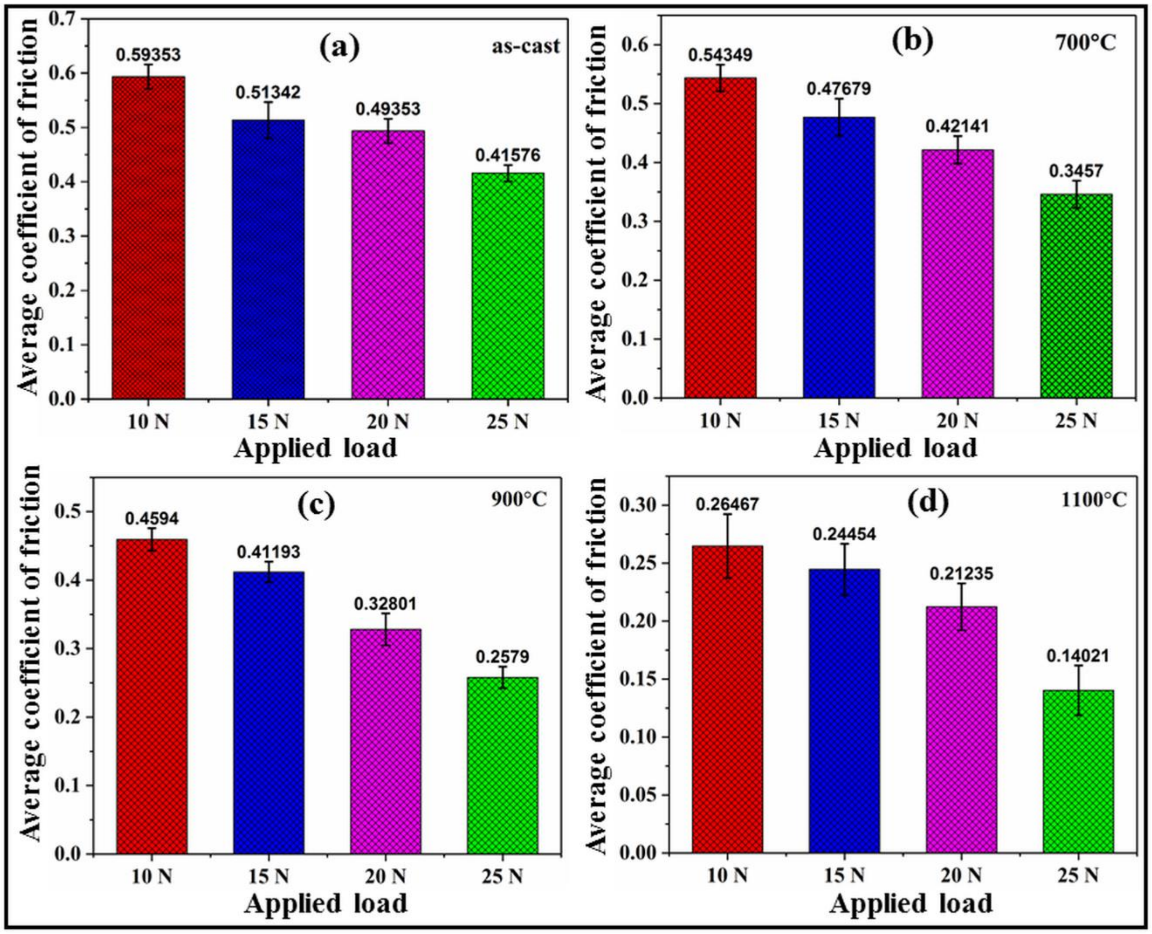

Figure 5.7 Average coefficient of friction with varying applied normal load of $Ti_{35}Zr_{35}Nb_{15}Mo_5Fe_5Cr_5$ CCA in SBF solution for (a) as-cast, and annealed at (b) 700°C, (c) 900°C, and (d) 1100°C specimens.

Figure 5.8 (a-d) illustrates the variation in specific wear rate (SWR) with sliding time of the $Ti_{35}Zr_{35}Nb_{15}Mo_5Fe_5Cr_5$ CCA under different normal loads in SBF solution. At a normal load of 10 N and a sliding time of 30 minutes, the as-cast CCA exhibits an SWR of 1.53×10^{-7} mm^3/N.mm. As the sliding time increases to 90 minutes, the SWR increases sharply, followed by a gradual increase beyond this point. This behavior may be attributed to a progressive increase in tribo-surface temperature during prolonged sliding, which facilitates the formation of hard, smooth oxide layers that contribute to surface protection.

In addition, at lower loads and lesser sliding durations, two-body abrasive or plowing wear is the predominant wear mechanism. In contrast, with prolonged sliding, the dominant wear mechanism changes to a combination of abrasive and oxidative wear. Figure 5.8 (a) shows the influence of applied load on the specific wear rate (SWR) of the as-cast CCA. The observed trend closely follows Archard's Law [197], which establishes a direct relationship between SWR and applied pressure. As applied pressure increases proportionally with load, a higher load consequently results in an increased SWR.

As described by Archard's law [197], the SWR is inversely related to the material's hardness. Since annealing at elevated temperatures enhances hardness, a corresponding decrease in SWR is observed. The CCA annealed at 1100°C exhibits an SWR of 7.27×10^{-8} $mm^3/N.mm$ under a 10 N normal load and 30 minutes of sliding, as shown in Figure 5.8 (d). In addition, as the sliding time increases up to 90 minutes, the SWR of the 1100 °C-annealed CCA gradually increases, after which it increases very slowly. Similar to the as-cast condition, the SWR of the annealed CCA also increases with higher normal loads and longer sliding times; however, the rate of increase is noticeably slower. Notably, the SWR values of both the as-cast and annealed CCA specimens are considerably lower than those reported for other refractory HEAs, such as $Ti_xZrNbTaMo$ (x = 0.5, 1, 1.5, and 2), as well as the Ti6Al4V alloy [198].

Figure 5.9 exhibits SEM and AFM images of the worn surfaces of the as-cast $Ti_{35}Zr_{35}Nb_{15}Mo_5Fe_5Cr_5$ CCA after 120 minutes of sliding time. At 10 N, the worn surface of the as-cast CCA shows (Figure 5.9 (a)) pronounced plowing marks and a small delaminated region, indicating that abrasive and delamination wear are the dominant mechanisms under this load. In contrast, at 25 N, the worn surface of the as-cast CCA (Figure 5.9 (b)) reveals more delamination, fine cracks in the transverse direction, and adhesion of the wear scar.

Additionally, the presence of an oxide layer and shallower plow marks suggests that delamination, adhesion, and oxidative wear mechanisms become more prominent at higher loading conditions. Additionally, the AFM was conducted to analyze the worn surface and to correlate surface topography parameters with the wear rate. Figure 5.9 (c-d) shows the AFM surface topography of worn surface of the as-cast CCA under a 25 N applied load and 120 minutes of sliding. Surface roughness parameters, including average roughness (R_a), root mean square roughness (R_q), skewness (R_{sk}), and kurtosis (R_{ku}), were extracted from the AFM data, and the results are summarized in Table 5.1.

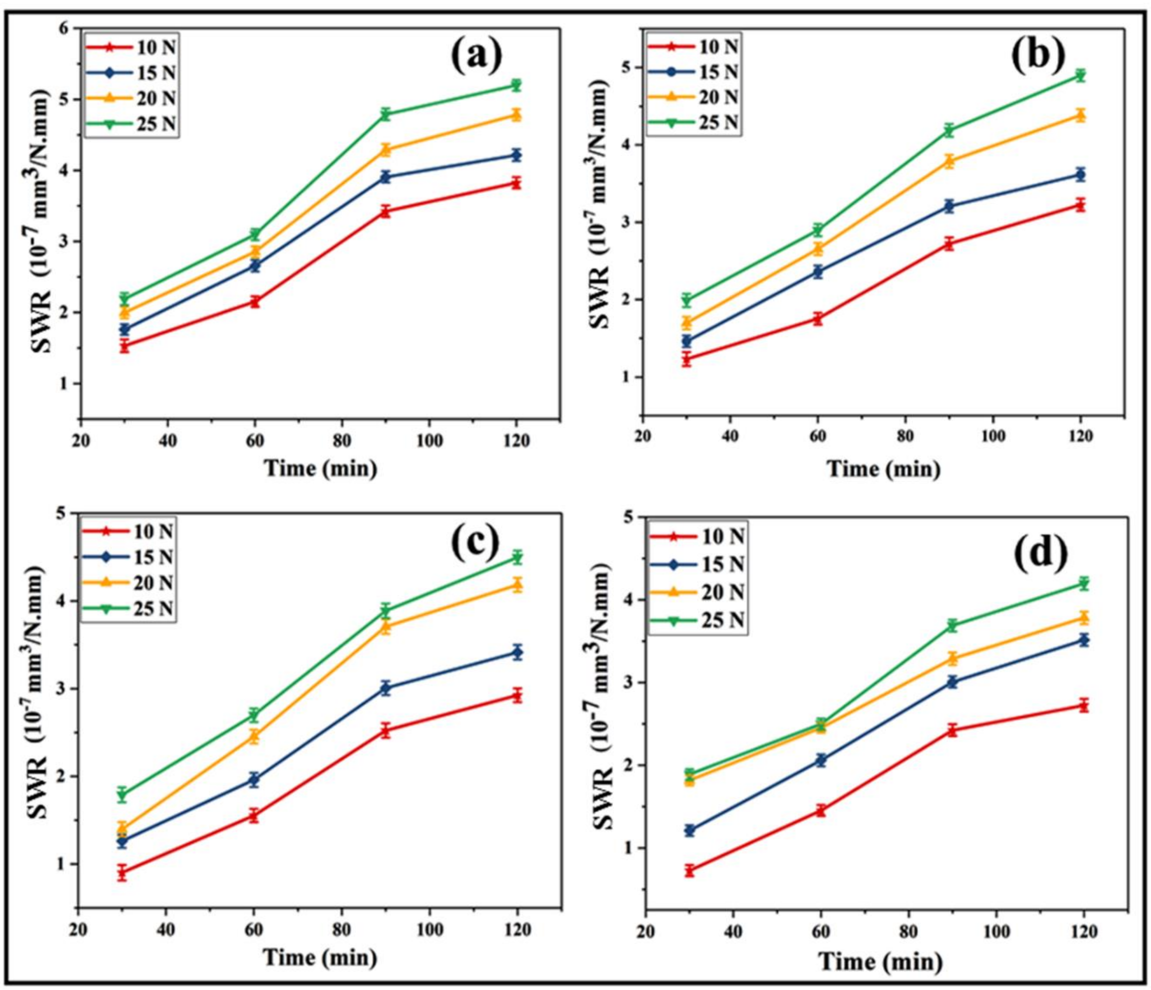

Figure 5.8 Effect of normal load on SWR with varying sliding time of $Ti_{35}Zr_{35}Nb_{15}Mo_5Fe_5Cr_5$ CCA in SBF solution for (a) as-cast and annealed at (b) 700°C, (c) 900°C, and (d) 1100°C specimens.

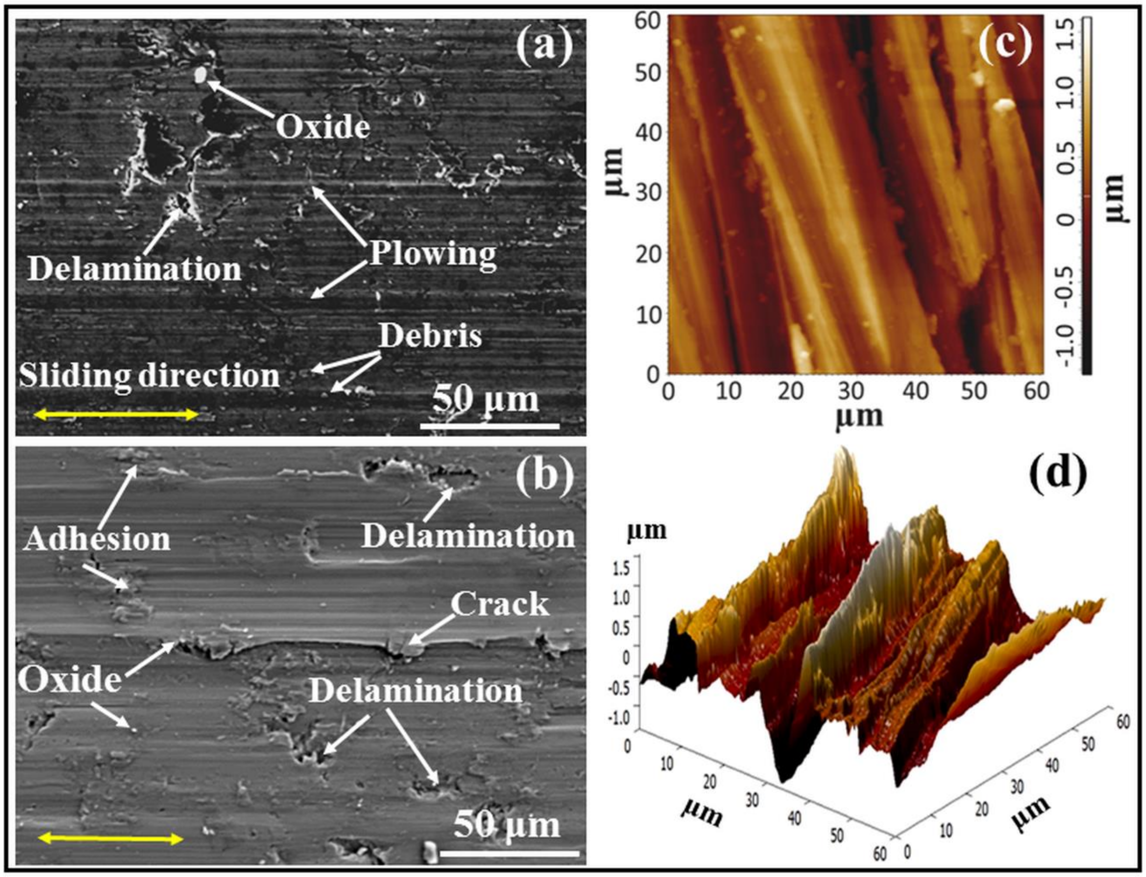

Figure 5.9 SEM and AFM images of the worn surface of the as-cast $Ti_{35}Zr_{35}Nb_{15}Mo_5Fe_5Cr_5$ CCA after 120 minutes of sliding: (a, b) SEM images under applied loads of 10 N and 25 N, respectively; (c, d) 2D and 3D AFM topography at 25 N load.

Table 5.1: Surface topography parameters of the $Ti_{35}Zr_{35}Nb_{15}Mo_5Fe_5Cr_5$ CCA at a 25 N applied load and 120 min sliding time.

Specimen	Average surface roughness (R_a)	Root mean square roughness (R_q)	Skewness (R_{sk})	Kurtosis (R_{ku})
as-cast CCA	0.310 µm	0.348 µm	0.223	3.288
700˚C annealed CCA	0.286 µm	0.317 µm	0.049	2.965

900˚C annealed CCA	0.259 µm	0.291 µm	- 0.097	2.606
1100˚C annealed CCA	0.109 µm	0.126 µm	- 0.190	2.224

Figure 5.10 (a-i) shows the SEM and AFM images of the worn surfaces of the annealed CCA after 120 minutes of sliding. SEM worn surface analysis of the annealed CCA reveals that the plowing-induced wear scars are shallower and finer compared to the as-cast material under a 10 N applied load. This improved wear resistance is attributed to the increased hardness due to annealing. At a higher load of 25 N, the worn surfaces of the CCA annealed at 700°C and 900°C display minor delaminated regions, signs of adhesion, and fine plow marks. Additionally, the CCA annealed at 1100°C, which possesses the highest hardness among the samples, experiences significant frictional heating during sliding against the hard counter ball, leading to an increase in the tribo-surface temperature. This elevated temperature facilitates the formation of a hard, smooth metallic oxide layer through the reaction of metallic elements with ambient oxygen, as seen in Figure 5.10 (h). Consequently, both the wear rate and COF of the 1100°C-annealed CCA are reduced.

The AFM 3D surface topography images of the worn surface of the annealed CCA at 25 N load and 120 minutes sliding time are shown in Figure 5.10 (c, f, and i), and surface topography parameters are presented in Table 5.1. Table 5.1 clearly indicates that the surface roughness of the annealed CCA is lower than that of the as-cast CCA. Additionally, surface roughness progressively decreases with increasing annealing temperature. This trend may be attributed to the enhanced hardness of the annealed CCA, which hinders the development of deep grooves during wear, resulting in a smoother surface. Similar findings were reported by Ezatpour and Parizi for the $CoCrFeNiMoTi_x$ CCA system [199].

R_{sk} characterizes the asymmetry of a surface profile relative to its mean plane and is commonly used to assess a material's load-bearing capacity. A negative R_{sk} value is indicative of enhanced load-bearing performance. As shown in Table 5.1, Rsk decreases with increasing annealing temperature, suggesting that the load-bearing capacity of the CCA improves upon annealing. In contrast, R_{ku} measures the sharpness of surface features, specifically, the peaks and valleys relative to the mean plane. A R_{ku} value greater than 3 indicates a spiky surface, while a value below 3 suggests a more rounded, bumpy surface [200]. The as-cast CCA exhibits a R_{ku} value above 3, whereas the annealed samples show values below 3, as presented in Table 3. This indicates that annealing results in a transition to bumpy surface features. Such bumpy surfaces, with their irregular protrusions, are beneficial as they promote more uniform load distribution during sliding, thereby minimizing localized wear.

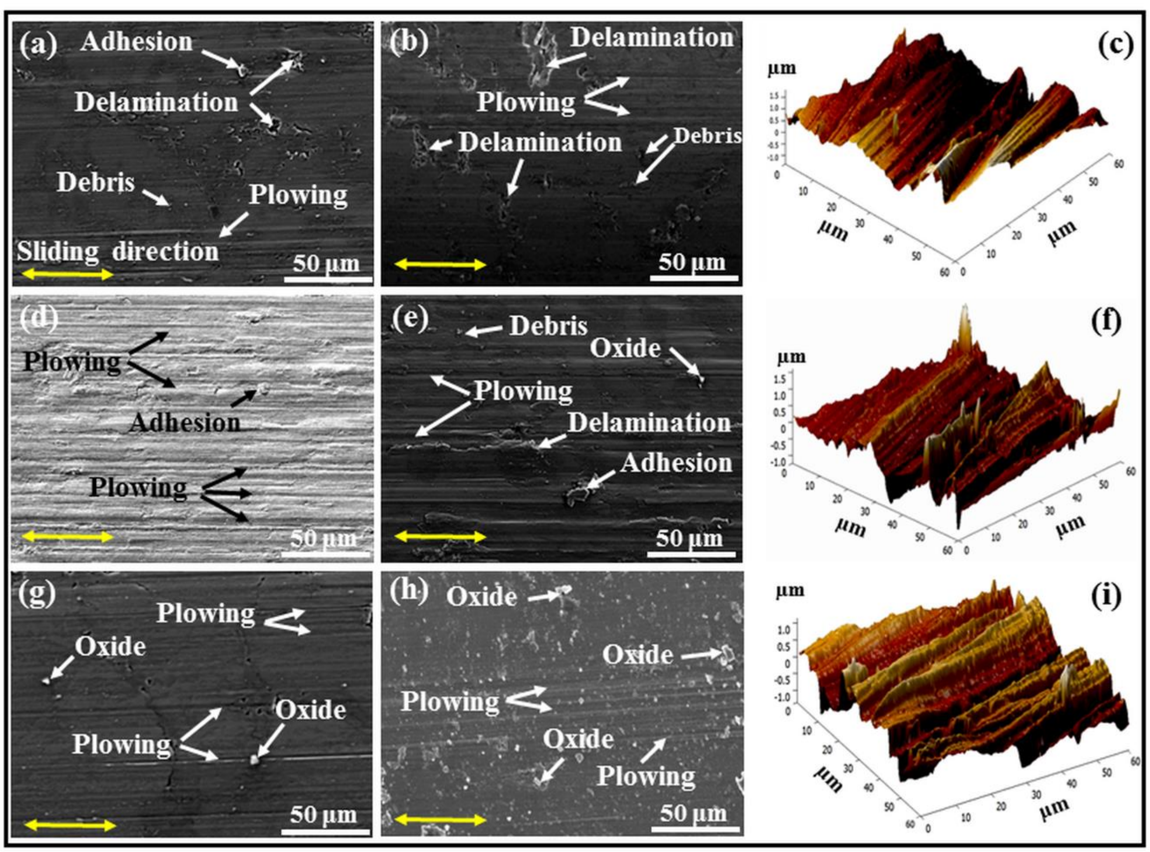

Figure 5.10 SEM and AFM characterization of the worn surface of the annealed $Ti_{35}Zr_{35}Nb_{15}Mo_5Fe_5Cr_5$ CCA after 120 minutes of sliding time: (a, d, g) SEM images at 10 N applied load, and (b, e, h) SEM images at 25 N applied load for samples annealed at 700°C, 900°C, and 1100°C, respectively; (c, f, i) corresponding AFM 3D topography images at 25 N applied load for the 700°C, 900°C, and 1100°C annealing temperature.

5.3 Discussion

Further discussion of the results presented in the previous section is necessary to assess the potential of the $Ti_{35}Zr_{35}Nb_{15}Mo_5Fe_5Cr_5$ CCA as a biomaterial.

5.3.1 Applicability of the empirical model for predicting phase stability and phase evolution of the $Ti_{35}Zr_{35}Nb_{15}Mo_5Fe_5Cr_5$ CCA

As previously discussed, in multicomponent alloys, several thermo-physical parameters, such as entropy (ΔS_{mix}), mixing enthalpy (ΔH_{mix}), atomic size mismatch (δ), valence electron concentration (VEC), Ω parameter, and electronegativity difference ($\Delta\chi_p$)—are commonly utilized to predict phase formation in HEAs/CCAs [201]. Using the Miedema model [176], the binary mixing enthalpies of the elements in the $Ti_{35}Zr_{35}Nb_{15}Mo_5Fe_5Cr_5$ CCA were determined and are shown in Figure 5.11. However, to estimate the alloy's overall mixing enthalpy, a regular solution model was applied, while additional thermo-physical parameters were assessed following the method proposed by Guo et al. [56]. As shown in Table 5.2, the computed values for these parameters fall within the accepted criteria for BCC solid solution formation in multicomponent alloys, with the exception of the atomic size difference.

In the $Ti_{35}Zr_{35}Nb_{15}Mo_5Fe_5Cr_5$ CCA, the atomic size difference (δ) exceeds the standard value of 6.6%, indicating a considerable amount of lattice distortion energy. This distortion destabilizes the solid solution phase and facilitates the formation of the Laves phase, which typically follows an AB_2 stoichiometry. Notably, when the effective atomic radius ratio (r_A/r_B) falls within the range of 1.05 to 1.70, a C14-type Laves phase is likely to form [178]. In the present alloy, the r_{Ti}/r_{Cr} ratio is 1.169, which suggests the formation of a C14-type Laves phase along with BCC solid solution phase. In addition, XRD analysis also confirms the present CCA consists of two BCC solid solution phases along with C14-type Laves phase. The lattice parameters of the BCC1 and BCC2 phases are very similar to those of Nb and Zr, respectively, suggesting that Nb and Zr act as the host lattices in these phases. The host lattice concept was explained by taking into account the bond strength and melting temperatures of the elements in multicomponent alloys [202].

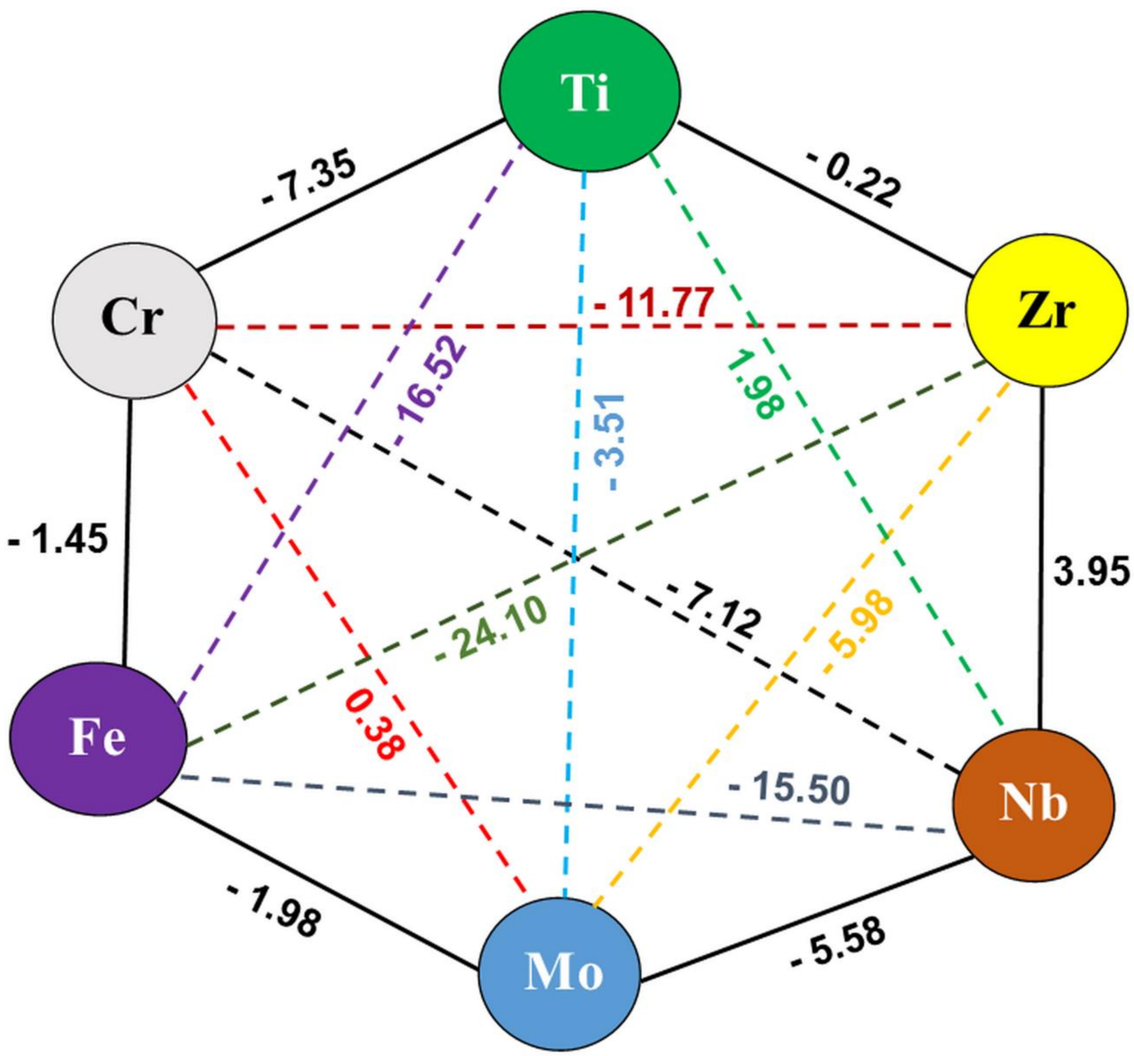

Figure 5.11 Binary mixing enthalpy (kJ/mol) values of all the pairs of elements in $Ti_{35}Zr_{35}Nb_{15}Mo_5Fe_5Cr_5$ CCA.

Table 5.2: Thermodynamic parameters along with criterion for the evolution of solid solution in HEAs and their calculated values for the present $Ti_{35}Zr_{35}Nb_{15}Mo_5Fe_5Cr_5$ CCA.

Parameter	Solid solution formation criterion [56, 174,198-199]	$Ti_{35}Zr_{35}Nb_{15}Mo_5Fe_5Cr_5$ CCA
ΔS_{mix} (J/mol.K) $$\Delta S_{mix} = -R\sum_{i=1}^{n} C_i \ln C_i$$	$11 \leq \Delta S_{mix} \leq 19$	12.23
ΔH_{mix} (kJ/mol) $$\Delta H_m = \sum_{i=1, i\neq j}^{n} \Omega_{ij} C_i C_j$$	$- 22 \leq \Delta Hmix \leq 7$	- 3.248
Ω (dimensionless) $$\Omega = \frac{T_m \Delta S_{mix}}{\lvert\Delta H_{mix}\rvert}$$	$\Omega > 1.1$	8.21
δ (%) $$\delta[\%] = 100 \cdot \sqrt{\sum_{i=1}^{n} C_i \left(1 - \frac{r_i}{\bar{r}}\right)^2}$$	$\delta \leq 6.6$	7.38
VEC (dimensionless) $$VEC = \sum_{i=1}^{n} C_i (VEC)_i$$	VEC < 6.87; BCC 6.87 < VEC < 8.0; BCC + FCC VEC ≥ 8; FCC	4.55

5.3.2 Mechanical properties of $Ti_{35}Zr_{35}Nb_{15}Mo_5Fe_5Cr_5$ CCA

5.3.2.1 Strengthening mechanisms of $Ti_{35}Zr_{35}Nb_{15}Mo_5Fe_5Cr_5$ CCA

As discussed in Section 5.2.3, the hardness and YS of the $Ti_{35}Zr_{35}Nb_{15}Mo_5Fe_5Cr_5$ CCA deviate from the values predicted by the mixture rule based on its constituent elements. According to this rule, the expected values calculated using $(\mathrm{HV})_{\mathrm{mix}} = \sum_{i=1}^{n} c_i \cdot \mathrm{HV}_i$ and $(\sigma_y)_{\mathrm{mix}} = \sum_{i=1}^{n} c_i \cdot (\sigma_y)_i$, where c_i, HV_i, and σ_{y_i} represent the atomic concentration, hardness, and yield strength of each element, are 1.013 GPa and 224.35 MPa, respectively. More accurate methods reported in the literature for estimating yield strength and hardness are based on micromechanics approaches such as Mori-Tanaka [203] and self-consistent methods [204]. Self-consistent approach yielded the hardness and yield strength values of the CCA to be 1.03 GPa and 234.60 MPa, respectively, which are very close to the predictions obtained from the rule-of-mixtures approach. In contrast, the experimentally measured hardness and estimated YS of the as-cast alloy are significantly higher, at 6.31 GPa and 1203.94 MPa.

This indicates that the exceptional strength of the alloy likely results from a combination of solid solution and precipitation strengthening mechanisms. In metallic solid solutions, solid solution strengthening occurs through elastic interactions between the localized stress fields of solute atoms. The contribution to strength from this mechanism increases with increasing atomic size and modulus mismatches. Additionally, the presence of secondary phase particles appears to play a crucial role. The widespread distribution of such particles, including Laves phases, impedes dislocation motion, which in turn can significantly enhance the overall strength of the alloy.

5.3.2.2 Mechanical properties of the present CCA compared to other reported implant biomaterials

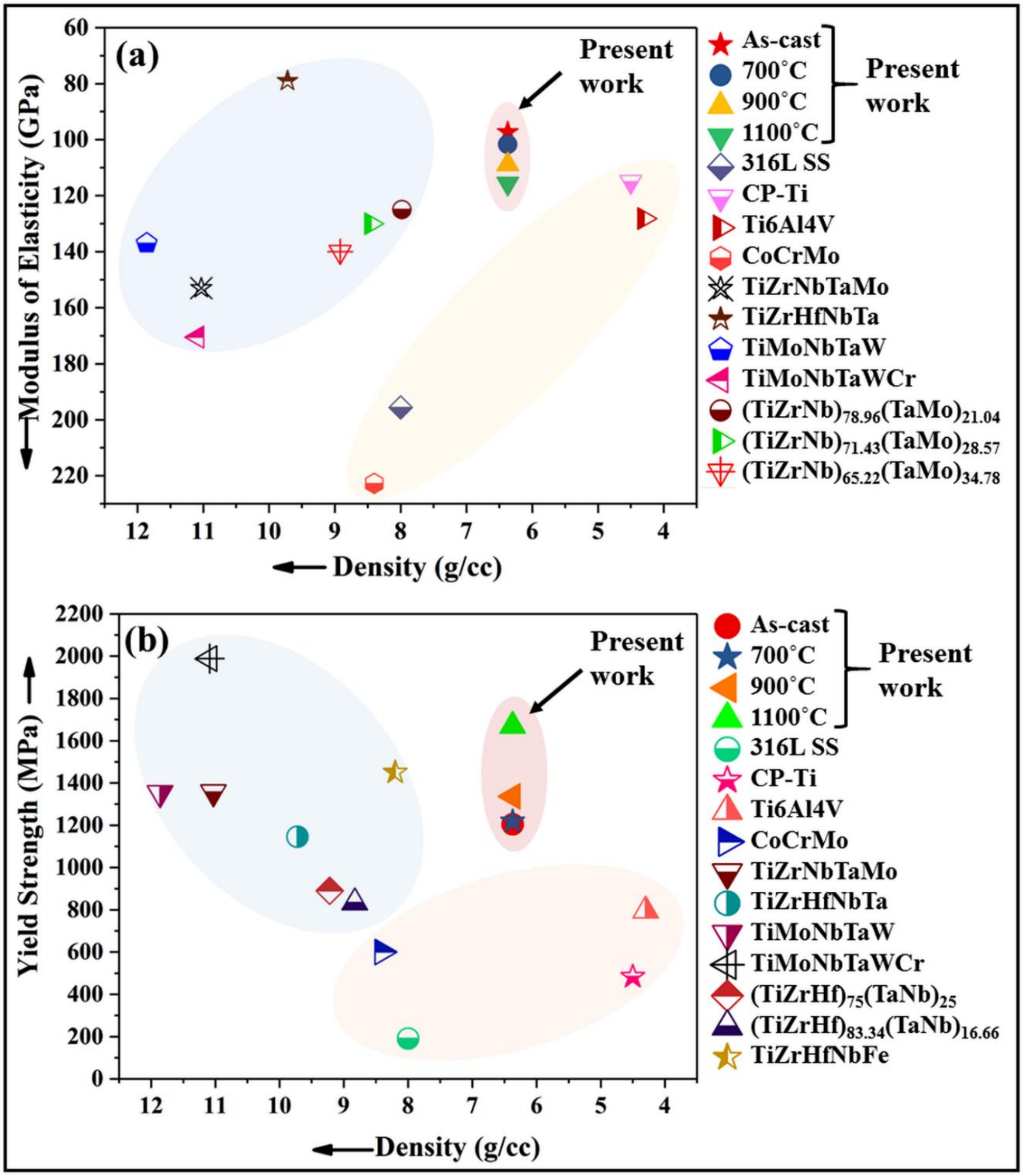

Figure 5.12 Comparison of the present work with some conventional biomaterials and other biocompatible HEAs/CCAs (a) modulus of elasticity vs density and (b) yield strength vs density.

Mechanical properties are widely recognized as critical factors in the evaluation of implant biomaterials, as replacement prosthetic components are subjected to complex loading conditions throughout their operational lifespan. Figure 5.12 compares the mechanical properties, specifically elastic modulus, yield strength, and density, of the $Ti_{35}Zr_{35}Nb_{15}Mo_5Fe_5Cr_5$ CCA with those of various traditional biomaterials and other biocompatible HEAs/CCAs reported in the previous studies [42,63,67,69,122,191,205-206]. The present CCA demonstrates an outstanding combination of low density, low elastic modulus, and high YS, compared to the various existing conventional and high-entropy biomaterials.

5.3.3 Wear resistance of $Ti_{35}Zr_{35}Nb_{15}Mo_5Fe_5Cr_5$ CCA

Orthopedic implant biomaterials used in joint replacements are unavoidably subjected to wear, which plays a critical role in determining the longevity of the implant. Therefore, high wear resistance is essential, as insufficient wear resistance can generate wear particles and subsequent particle-induced diseases. Traditional titanium-based alloys typically exhibit low wear resistance, which can lead to the release and accumulation of potentially cytotoxic elements, such as Al and V [67]. This limitation poses a significant challenge to their long-term use in joint replacement applications.

The $Ti_{35}Zr_{35}Nb_{15}Mo_5Fe_5Cr_5$ CCA demonstrates outstanding strength and hardness, attributed to its substantial atomic size mismatch and the formation of hard Laves phase particles. These findings are consistent with Archard's Law [197], which indicates a strong relationship between a material's hardness and its wear resistance. Enhanced hardness improves the material's capacity to resist surface plastic deformation, thereby limiting the formation of microcracks. This, in turn, improves wear resistance and supports the material's long-term suitability for biomedical applications. Notably, the wear resistance of the present CCA is markedly superior to that of other biocompatible HEAs and conventional alloys, such as $TiZrHfNbFe_x$ (x = 0 - 2) [67], $Ti_xZrNbTaMo$ (x = 0.5, 1, 1.5, and 2) [198], 316L SS, cp-Ti, and Ti6Al4V [207].

5.3.4 Cost analysis of the present $Ti_{35}Zr_{35}Nb_{15}Mo_5Fe_5Cr_5$ CCA

The overall cost of an alloy used to manufacture a component for a specific application is mainly influenced by the cost associated with its raw materials and processing. While the chosen fabrication method can affect the actual production cost, a preliminary estimate based on the prices of the constituent elements remains useful. For a given application, such as biomedical use in this case, assuming a standard fabrication process allows for a comparative estimate of the relative cost against existing/standard materials and other emerging potential materials.

Figure 5.13 exhibits a comparison of relative cost versus specific yield strength (YS/density) for the $Ti_{35}Zr_{35}Nb_{15}Mo_5Fe_5Cr_5$ CCA, along with various reported biocompatible HEAs/CCAs and conventional biomedical materials. Although the cost of this CCA exceeds that of 316L SS and cp-Ti, but it is comparable to the cost of the Ti6Al4V alloy. Notably, the cost of the present CCA is considerably lower than that of other biocompatible HEAs/CCAs. In addition, its specific strength is significantly higher than that of both biocompatible HEAs/CCAs and traditional biomedical materials. These attributes demonstrate the $Ti_{35}Zr_{35}Nb_{15}Mo_5Fe_5Cr_5$ CCA as a promising candidate for biomedical applications due to its favorable combination of cost and mechanical performance.

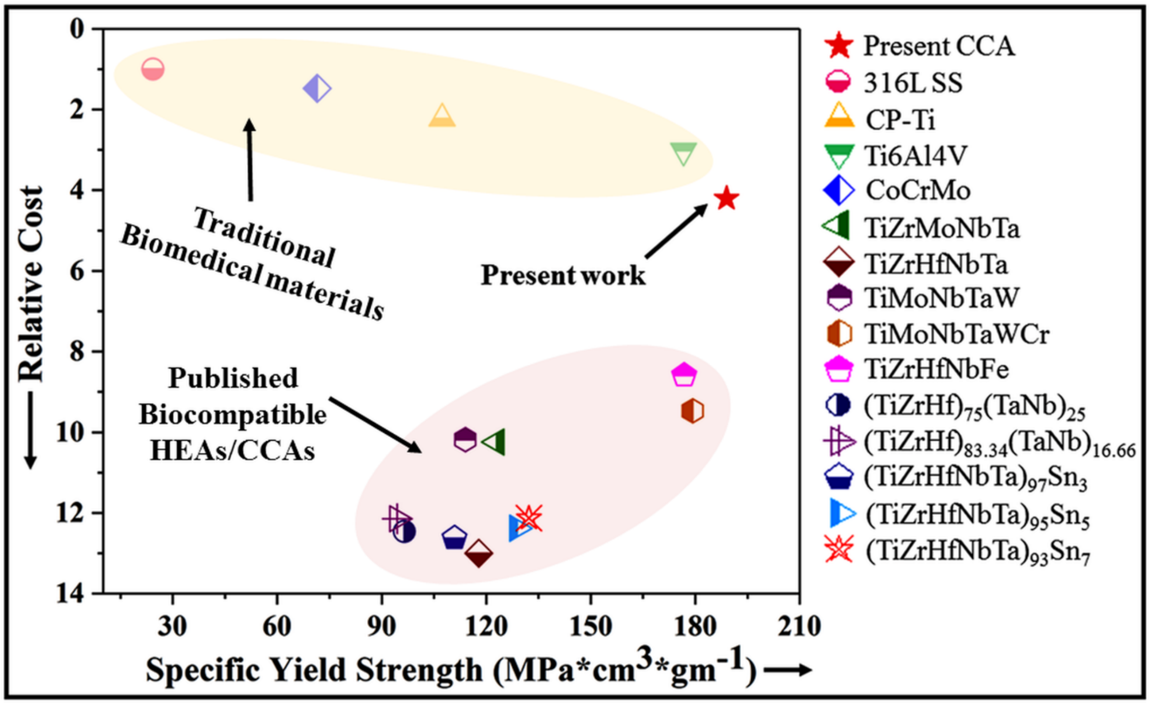

Figure 5.13 Relative cost (with respect to the cost of 316L SS) versus specific yield strength of the $Ti_{35}Zr_{35}Nb_{15}Mo_5Fe_5Cr_5$ CCA and comparison with various biocompatible HEAs/CCAs, as well as with conventional alloys.

5.4 Summary

This chapter presents a successful attempt to develop a new CCA with potential for biomedical applications. The phase evolution, mechanical properties, and tribological behaviour of as-cast and annealed $Ti_{35}Zr_{35}Nb_{15}Mo_5Fe_5Cr_5$ CCA were systematically investigated. The key findings from this chapter are summarized below.

i. The newly developed $Ti_{35}Zr_{35}Nb_{15}Mo_5Fe_5Cr_5$ CCA, synthesized using a vacuum arc melting furnace, consists of two BCC solid solution phases (a_{BCC1} = 3.360 Å and a_{BCC2} = 3.616 Å) along with a $TiCr_2$-type Laves phase in its as-cast state. This alloy has a density of 6.37 g/cm³, which is lower than that of 316L SS and significantly lower than the reported biocompatible HEAs/CCAs.

ii. The dendritic microstructure observed in the as-cast CCA changed into a predominantly globular structure after annealing. In addition, increasing the annealing temperature resulted in an increased volume fraction of the Laves phase.

iii. The as-cast CCA exhibits average hardness, yield strength, and elastic modulus values are 618.39, 1203.94 MPa, and 97.32 GPa, respectively. In the case of annealed CCA, these values increase with increasing annealing temperature, attributed to a greater amount of the hard Laves phase. Specifically, 1100°C annealed CCA depicts the average hardness of 833.08 and a yield strength of 1669.65 MPa. Elastoplastic analysis reveals that, although the strength increases with a higher content of the hard Laves phase, the alloy maintains its plasticity without significant reduction.

iv. Wet wear tests demonstrated that the as-cast $Ti_{35}Zr_{35}Nb_{15}Mo_5Fe_5Cr_5$ CCA possesses considerably good wear resistance (SWR = 1.53×10^{-7} mm³/N.mm) under a 10 N load and 30-minute sliding duration in SBF solution. Annealing further improved the wear resistance by promoting the formation of hard Laves phases, which contributed to increased material hardness. The alloy annealed at 1100°C showed the highest wear resistance (SWR = 7.27×10^{-8} mm³/N.mm) under a 10 N load and 30-minute sliding time.

v. Worn surface analysis reveals that delamination is the dominant wear mechanism in the as-cast CCA, whereas abrasive and oxidative wear are predominant in the alloy annealed at 1100°C